ACS Energy LETTERS

http://pubs.acs.org/journal/aelccp

Waxing Bare High-Voltage Cathode Surfaces to Enable Sulfide Solid-State Batteries

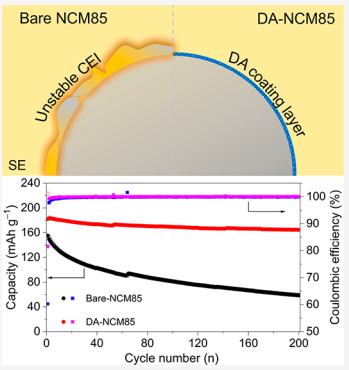
Yangyang Huang,[§] Laidong Zhou,[§] Chang Li, Zhuo Yu, and Linda F. Nazar*

Cite This: *ACS Energy Lett.* 2023, 8, 4949−4956

Read Online

ACCESS | Metrics & More | Article Recommendations | Supporting Information

ABSTRACT: Ni-rich cathode materials (i.e., $LiNi_xCo_yMn_{1-x-y}O_2$, $x \geq 0.8$) coupled with sulfide solid catholytes such as argyrodite (Li_6PS_5Cl) are promising materials for high-performance solid-state batteries. However, the chemical reactivity and electrochemical decomposition of argyrodite above 2.5 V cause fast capacity fading in the operating window of the cell, necessitating the use of coatings to suppress those reactions. Here, we report a simple organic-coating concept that generates an electronically insulating cathode−electrolyte interphase which stabilizes the argyrodite against oxidative degradation. Utilizing Li_6PS_5Cl as the solid electrolyte, the nanometric layer of "waxy soap" (fatty acid salt) coated on the cathode active material (CAM) enables a capacity retention of 90% after 200 cycles (2.8−4.3 V vs Li^+/Li), compared to 38% retention for the bare CAM, confirming both its interfacial stability and permeability to Li ions. This emphasizes the suitability and potential of this low-cost, easily processable, flexible, and conformal coating to suppress interfacial degradation in sulfide-based composite cathodes.

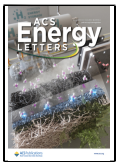


Global decarbonization relies on substantially reducing the worldwide energy dependence on fossil fuels and increasing the use of renewable energy resources. Rechargeable batteries are a key component to realize the widespread use of clean energy.[1,2] While organic liquid electrolytes in conventional lithium-ion batteries present potential safety concerns for large-scale electricity storage, all solid-state batteries (ASSBs) have the potential to provide higher energy density and better safety.[3,4] Their advantages also stem from a wider range of thermal stability and lack of viscosity-dependent changes in conductivity at low temperatures owing to the nature of the inorganic solid electrolytes.

A wide range of inorganic solid electrolytes (SEs) have been studied, including oxides, sulfides, and chlorides.[5−7] Among them, sulfides exhibit the highest ionic conductivity[8−11] (up to 32 $mS \cdot cm^{-1}$), and some sulfides have been suggested to form a quasi-stable interface with a Li metal anode.[12] Moreover, their features of good elasticity and softness can enable facile processing methods, such as cold-pressing and intimate interfacial contact with the cathode active material (CAM). Nevertheless, they display a low oxidation potential of ∼2.5 V vs Li^+/Li.[13] Thus, sulfide materials are suitable as a solid electrolyte layer with a protected Li metal anode and a low voltage cathode, such as S/Li_2S.[14,15] However, with high-voltage positive electrodes, the reaction at the junction between an oxidizable sulfide SE and typical CAMs prone to oxygen release above 4.2 V causes the formation of an unfavorable interface layer, resulting in resistance build-up and poor electrochemical performance.[16,17] Such instability has become one of the critical scientific issues hampering the commercialization of lithium thiophosphate-based ASSBs.

Constructing a buffer layer on the CAMs surface can enhance interfacial stability by preventing direct contact between the CAM and sulfide SE.[18,19] An ideal buffer should have favorable characteristics that include low electronic and high ionic conductivity in addition to being thin and homogeneous. Such a coating will enhance the cycling performance by suppressing decomposition reactions and hence lowering the charge-transfer resistance. To date, typical inorganic oxide coating materials, such as $Li(Nb/Ta)O_3$,[20−22] Li_2ZrO_3,[23] Li_2SiO_3,[24] $Li_4Ti_5O_{12}$,[25] Li_2CO_3, and their mixtures,[26−28] have been successfully proven to alleviate the interfacial degradation between CAMs and sulfide SEs, reflected by better cycling life. However, the complex (wet chemical and sol−gel) coating methods used for preparing the above-mentioned coatings employ extensive annealing and drying steps. Because of this, the processing can be costly and time-consuming and can yield nonhomogeneous films, making it less favorable for large-scale industrial applications. In addition, the high Young's modulus of the inorganic-coating materials mentioned above can lead to fracture and loss of

Received: August 17, 2023
Revised: September 29, 2023
Accepted: October 20, 2023
Published: November 1, 2023



Downloaded via CITY UNIV OF HONG KONG on August 23, 2025 at 12:24:52 (UTC).
See https://pubs.acs.org/sharingguidelines for options on how to legitimately share published articles.

© 2023 American Chemical Society

https://doi.org/10.1021/acsenergylett.3c01717
ACS Energy Lett. 2023, 8, 4949−4956

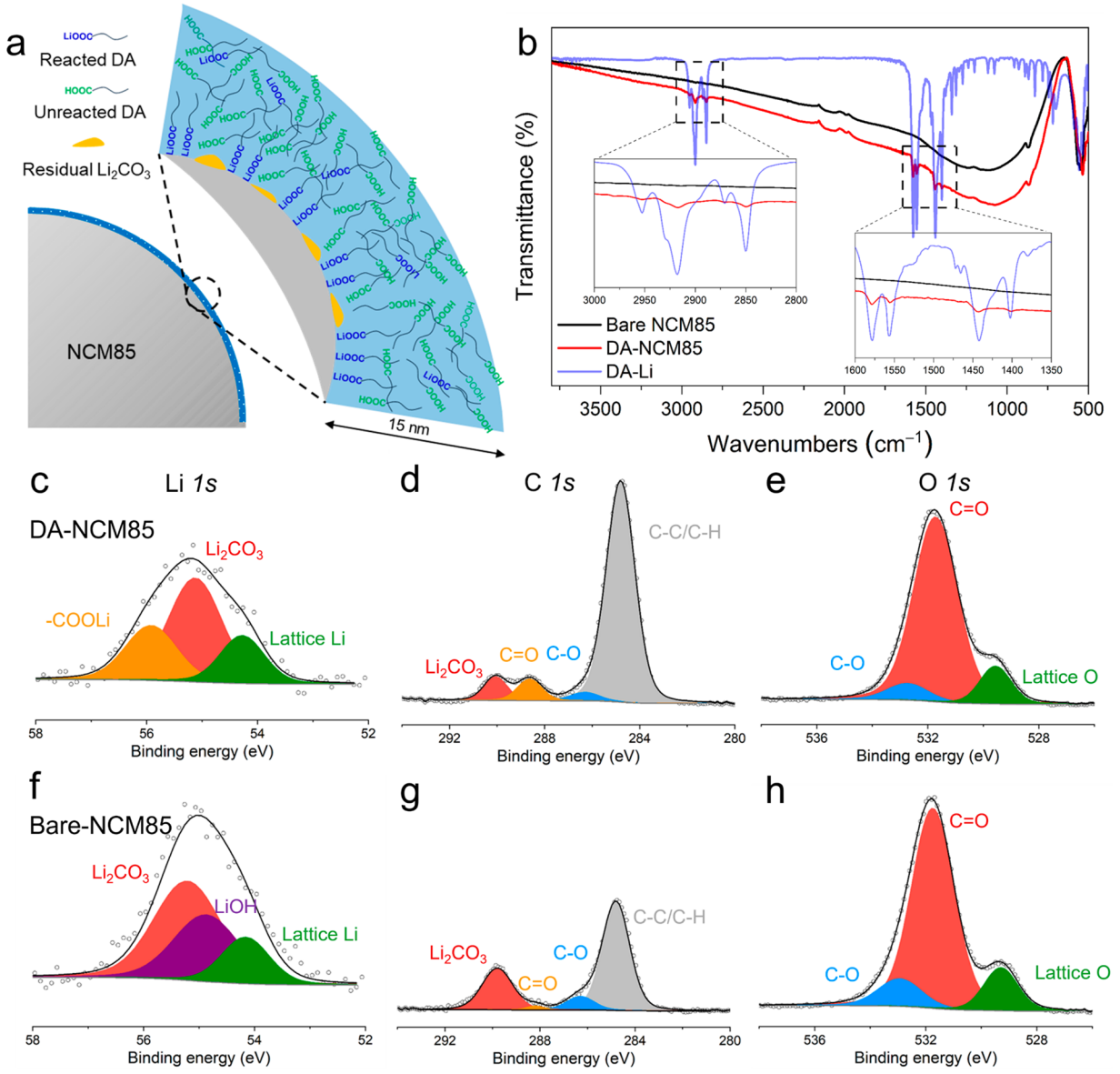


Figure 1. (a) Schematic depiction of surface (coating) structure for DA-NCM85; (b) FT-IR spectra; (c–h) XPS Li 1*s*, C 1*s*, and O 1*s* spectra of bare NCM85 and DA-NCM85. In panel f, contributions from Li_2CO_3 (55.1 eV) and LiOH (54.9 eV) slightly overlap. In panels d and g, the peak at 284.8 eV (C–C/C–H) arises from adventitious carbon contamination and provides the reference. The XPS spectra for the same element are on the same intensity scale.

contact with the NCM particles upon redox contraction/expansion during cycling.[29] Fairly simple, cost-effective, "plastic", and easily scalable coating methods and stable coating materials are required.

Organic acids with carboxyl (−COOH) functional groups react with residual lithium compounds on the Ni-rich cathode surface to form an organic lithium layer that improves NCM interface stability in traditional liquid electrolytes.[30,31] Nonetheless, this layer is partly soluble in organic alkyl carbonates, resulting in only a modest improvement in electrochemical performance. Taking advantage of the properties of the solid state, herein, we utilize a simple treatment of Li-$Ni_{0.85}Co_{0.1}Mn_{0.05}O_2$ (NCM85) with decanoic acid (DA) to form a nanometric coating layer. Importantly, the whole process is simple and achieved under an ambient atmosphere without any high-temperature sintering, allowing for mass production of DA-coated NCM for commercialization. The coating forms a natural cathode-electrolyte interphase (CEI), stabilizing the argyrodite–NCM85 interface to a high potential (4.3 V). Consequently, DA-coated NCM85 using Li_6PS_5Cl solid electrolyte at typical ASSB cell loading levels of ∼1.8 mAh/cm^2 delivers capacity retention of 90% after 200 cycles (2.8–4.3 V vs Li^+/Li) at room temperature, over 3-fold higher compared to the bare NCM85 ASSB. Furthermore, DA-coated NCM85 ASSB with a high loading of 5 mAh/cm^2 exhibits a reversible capacity of ∼4.4 mAh/cm^2 and satisfactory cycling stability over 160 cycles. This conformal and flexible coating leads to comparable or even-better electrochemical performance compared to the-state-of-art inorganic material coatings.[20−28] Furthermore, implementation of a simple coating process and low-cost precursor may significantly advance production without raising the price of ASSBs.

The DA was deposited on the NCM85 surface by a simple wet coating (see the Supporting Information) on a lab bench

https://doi.org/10.1021/acsenergylett.3c01717
ACS Energy Lett. 2023, 8, 4949−4956

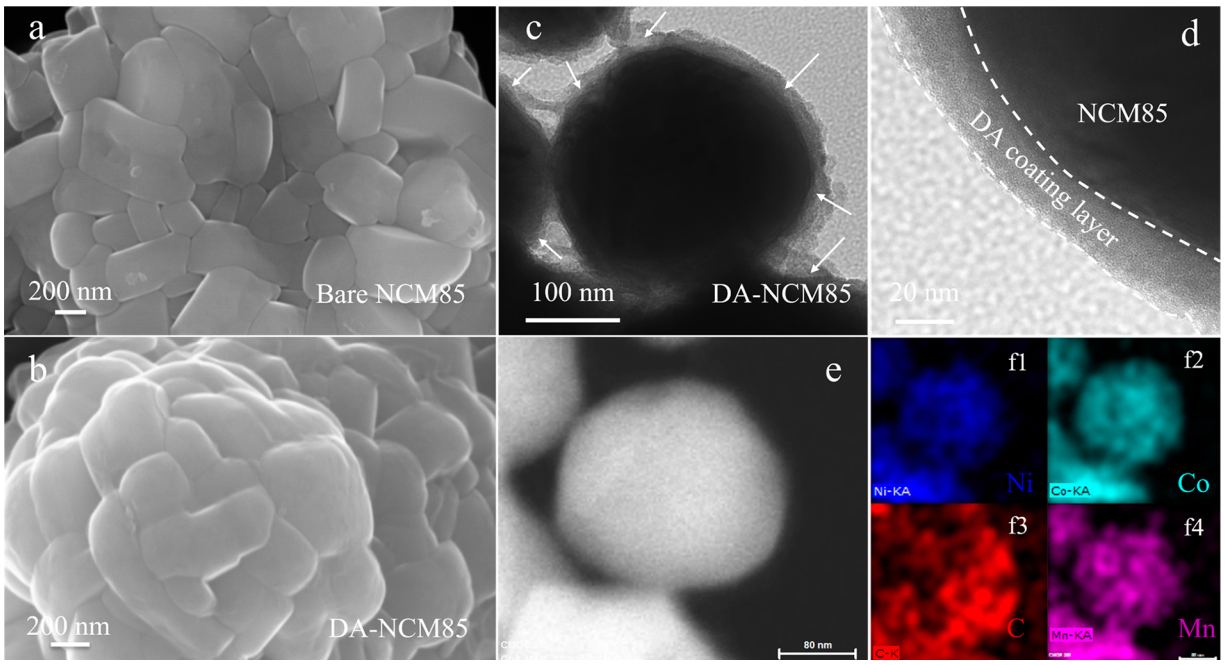


Figure 2. SEM images of (a) bare NCM85 and (b) DA-NCM85. (c) Low- and (d) high-magnification TEM images of DA-NCM85. (e) HAADF-STEM image and (f) EDS mapping.

under ambient conditions. The fatty acid reacts with residual lithium hydroxide, commonly observed on the surface of high-Ni NCM85,[32,33] in polar solvents (ethanol) to generate a protective CEI layer comprised of multiple layers of the fatty acid soap (Li-decanoate, or Li-DA) and residual DA after complete evaporation of ethanol, as shown schematically in Figure 1a. The DA-coated NCM85 was dried at 120 °C under a vacuum to remove residual water and ethanol. The X-ray diffraction (XRD) patterns of bare NCM85 and DA-NCM85 (Figure S1) show there is no discernible difference between the two samples, and all of the diffraction peaks can be indexed to the hexagonal-type layered structure with the $R\bar{3}m$ space group. Fourier-transform infrared (FT-IR) spectra (Figure 1b) were used to confirm the successful coating procedure. Compared to bare NCM85, the FTIR spectrum of DA-NCM85 shows new peaks at about 3000−2800 cm^{-1} corresponding to stretching of methylene groups and 1600−1350 cm^{-1} corresponding to the stretching vibration of carbonyl group, which match to the peaks observed for DA-Li.[34] The O−H group stretching and bending in the regions of 3300−2500 and 1440−1395 cm^{-1} cannot be distinguished from C−H stretching and bending. The chemical state of the surface DA was further confirmed by X-ray photoelectron spectroscopy (XPS) analysis (Figure 1c−h). Figure 1c,f shows that by comparison with bare NCM85, a new signal at 55.9 eV appears in the Li 1*s* spectrum of DA-NCM85, which corresponds to −COOLi species on the basis of literature reports (55.6−55.9 eV).[31,35,36] The presence of the alkyl carboxylate indicates that surface lithium hydroxide was consumed during the treatment process to form a layer of lithium decanoate. Residual Li_2CO_3 is still present at 55.1 eV,[37] while the appearance of a signal in the Li 1*s* spectrum attributable to the underlying $LiNi_{0.85}Co_{0.1}Mn_{0.05}O_2$[38] suggests the layer is quite thin (<10−15 nm and confirmed by TEM studies described below). In the C 1*s* spectrum (Figure 1g) of bare-NCM85, the peak at ∼289.9 eV corresponding to Li_2CO_3[38] is dominant. In the case of DA-NCM85 (Figure 1d), its intensity is much weaker, while C=O and C−H features from DA/Li are now evident with relatively high intensity. After DA-coating, the Li_2CO_3 on the surface of NCM85 is buried underneath the coating layer, and because XPS is highly surface-sensitive, the C 1*s* spectra show a decreased Li_2CO_3 peak intensity. Nonetheless, Li_2CO_3 may also be partly consumed by DA. The O 1*s* spectrum (Figure 1e,h) shows the DA/Li layer is nanometric as the underlying lattice oxygen is visible, in accord with the TEM results (see below).[39] Overall, these results indicate that the DA modification of NCM85 alters the surface's chemical properties to yield a thin layer rich in reacted DA-Li and remaining DA (Figure 1a), which is in good agreement with DA-modified NCM for liquid cells.[31]

Scanning electron microscopy (SEM) images (Figures 2a,b and S2) show that both bare NCM85 and DA-NCM85 have the same spherical morphology with a diameter of around 4 μm. These microspheres are aggregates of cuboid-like particles of several hundred nanometers in size. The high-magnification TEM images of DA-NCM85 show an ∼15 nm thick amorphous layer on the surface of NCM85 with 1.0 wt % DA coating (Figure 2c,d), compared to bare NCM85 (Figure S3), as illustrated schematically in Figure 1a. The DA/Li content of ∼0.96 wt % was determined by thermogravimetric (TG) analysis (Figure S4). Notably, there is minimal mass reduction at temperatures exceeding 400 °C, implying a limited Li_2CO_3 content on the surface of NCM85. When the coating fraction is increased to 2.0 wt %, the amorphous layer thickness exceeds 20 nm (Figure S5). With such a thick coating layer, Li ion diffusion can be significantly blocked due to the relatively low ionic conductivity of Li-DA (Figure S6). The carbon signal in the energy dispersive spectroscopy (EDS) mapping of the high-angle annular dark-field scanning transmission electron microscopy (HAADF-STEM) image of the 1.0 wt % DA-NCM85 (Figure 2e,f) indicates that DA/Li is uniformly distributed throughout the particle surface.

https://doi.org/10.1021/acsenergylett.3c01717
ACS Energy Lett. 2023, 8, 4949−4956

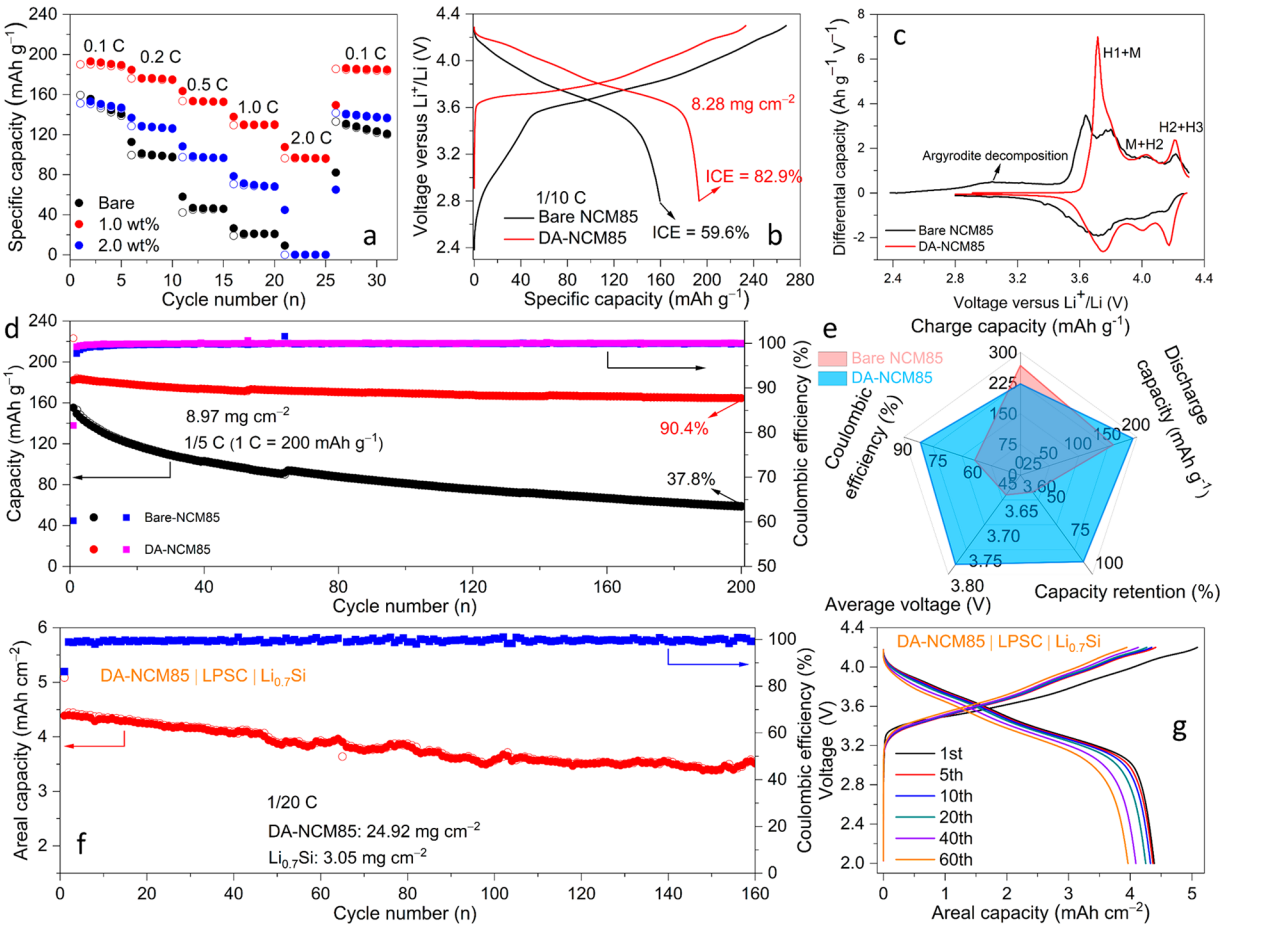


Figure 3. (a) Rate performance of bare NCM85 and DA-NCM85 with different coating content. (b) Initial charge/discharge profiles of bare NCM85 and 1 wt % DA-NCM85 at 0.1 C within the voltage range of 2.8−4.3 V vs Li^+/Li; (c) corresponding dQ/dV curves. (d) Cycling performance of bare NCM85 and 1 wt % DA-NCM85. (e) The radar image of the different electrochemical performance indicators for bare NCM85 and 1 wt % DA-NCM85. (f) Cycling performance and (g) corresponding voltage profiles of high-loading 1 wt % DA-NCM85 full cell with $Li_{0.7}Si$ anode.

The electronic and ionic conductivities of bare and DA-NCM85 were investigated by direct current (DC) polarization and electrochemical impedance spectroscopy (EIS) measurements. As shown in Figure S7a, the electronic conductivity drops after DA-coating and further decreases with increasing thickness of the coating due to the insulating nature of DA. In concert, an overall decrease in ionic conductivity is evident after DA coating as expected (Figure S7b).

To verify the effectiveness of the nanometric coating layer, the electrochemical performance of DA-coated NCM85 and bare NCM85 was investigated in SSBs by using commercial Li_6PS_5Cl (LPSC) SE and an In/LiIn anode. The particle size of argyrodite LPSC is ∼1 μm (D50) (Figure S8b). The XRD pattern of LPSC (Figure S8a) shows a single phase, and its ionic conductivity is 2.4 mS/cm (Figure S9) as measured by EIS. The cathode composite contained 80 wt % CAM (either bare NCM85 or DA-NCM85) and 20 wt % LPSC. Figure 3a shows the rate capability of bare NCM85, 1.0 and 2.0 wt % DA-NCM85 ASSBs. The bare-NCM85 cell exhibits the poorest rate performance: oxidation of LPSC at high voltage during cycling leads to the growth of insulating interphases on NCM85 and thus increased cell internal resistance. Both DA-NCM85 show enhanced rate performance compared with bare NCM85 due to the suppression of LPSC oxidation. The 1.0 wt % DA-NCM85 exhibits the best properties, while thicker coatings lead to poorer electronic and Li-ion percolation within the cathode composites. The 1.0 wt % DA-NCM85 cell delivers high discharge capacities of 190 to 130 mAh/g at 0.1 and 1.0 C, respectively. At an even higher C-rate of 2.0 C, it still delivers a discharge capacity of 97 mAh/g, while the bare NCM85 cell exhibits an inferior specific capacity of near zero. The electronic and ionic conductivity of cathode composites with bare-NCM85 and 1% DA-NCM85 were measured with DC polarization. During composite preparation, bare-NCM85 reacts with LPSC on contact due to their chemical incompatibility. This leads to the formation of an insulating interphase on NCM85 that inhibits electron transport between particles (Figure S10a). The Li ions mainly transport through LPSC within the composites, and thus, ionic conductivity is not significantly affected (Figure S10b). Therefore, the 1% DA-NCM85 composite exhibits much higher electronic conductivity and slightly lower ionic conductivity compared to the bare-NCM85 composite at its initial state before cycling. Furthermore, after cycling, the electronic and ionic percolation in the bare-NCM85 composite will be significantly blocked due to continuous LPSC oxidation. This explains the superior rate performance of 1% DA-NCM85 compared to bare NCM85.

Figure 3b displays the initial charge/discharge profiles of bare NCM85 and 1% DA-NCM85 at 0.1 C in a voltage range

https://doi.org/10.1021/acsenergylett.3c01717
ACS Energy Lett. 2023, 8, 4949−4956

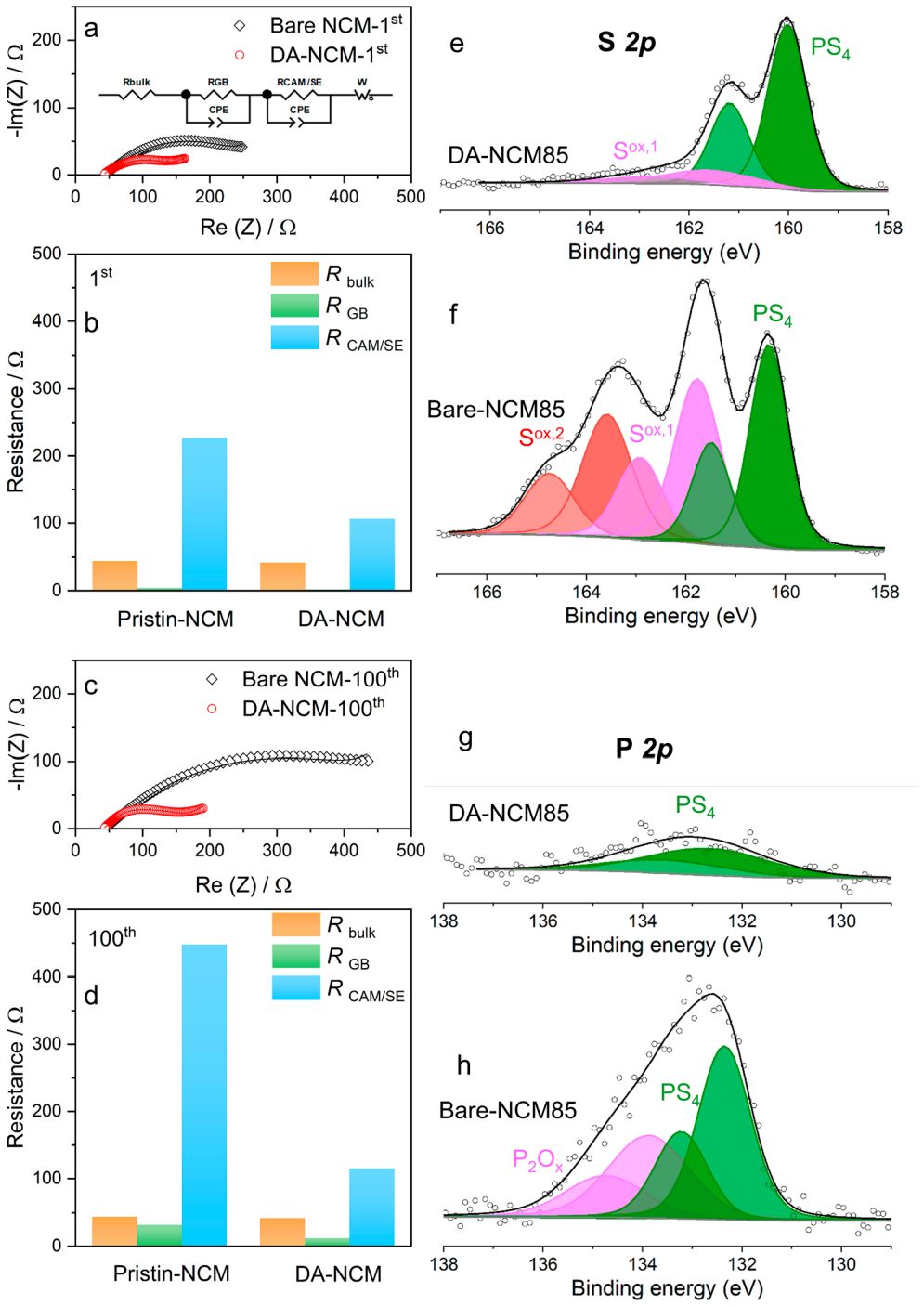


Figure 4. Nyquist plots of the electrochemical impedance bare NCM85 (black) and C-NCM85 (red) at (a) 1st and (c) 100th cycles in the discharged state. The inset in panel a exhibits the equivalent circuit used to fit the EIS data. (b, d) Summary of the fitting results. (e, f) S 2*p* and (g, h) P 2*p* XPS spectra of composite cathodes using DA-coated and bare NCM85 after 200 cycles, respectively. The spin doublet components are shaded with the same color for each spectrum.

of 2.18−3.68 V vs In/LiIn, corresponding to 2.8−4.3 V vs Li^+/Li. In comparison with bare NCM85, the DA-NCM85 cell delivered improved discharge capacity (190 vs 159 mAh/g) and a much higher initial Coulombic efficiency (ICE) (82.9% vs 59.6%), suggesting that the parasitic reactions at the NCM85|LPSC interface are suppressed by the DA coating during the initial charging process. In addition, there is an obvious slope below 3.0 V in the initial charging process for bare NCM85, corresponding to argyrodite (LSPC) decomposition, as previously reported.[40] This is due to the electronically conducting nature of NCM85; the addition of carbon to the cathode composite will lead to even more severe argyrodite decomposition.[41] This can also be observed in the corresponding d*Q*/d*V* profile of bare NCM85 in Figure 3c. The initial charge stage of DA-NCM85 does not show the same sloping voltage profile, showing that the DA coating effectively inhibits LSPC decomposition. From the d*Q*/d*V* curves of bare NCM85 and DA-NCM85 (Figure 3c), three redox peaks characterize the phase transitions from H1 to M, H2, and H3 phases during the de/lithiation process of

https://doi.org/10.1021/acsenergylett.3c01717
ACS Energy Lett. 2023, 8, 4949−4956

NCM85.[42] DA-NCM85 demonstrates a smaller voltage interval between the anodic−cathodic peak pairs and higher peak intensity than that of bare NCM85, suggesting improved electrochemical reaction activity induced by the stable NCM85|LPSC interface with the DA coating. The H1↔M anodic peak in the first cycle of DA-NCM85 slightly shifts to a high potential in comparison to bare NCM85, likely owing to increased impedance from the insulating surface modification layer. However, in the second cycle, DA-NCM85 shows better structural reversibility as evidenced by the similar peak shape and higher peak intensity (Figure S11).

The long-term cycling performance of bare-NCM85 and DA-NCM85 cells is shown in Figures 3d and S12. The DA-NCM85 cell maintains a high specific capacity of 166 mAh/g after 200 cycles at 0.2 C, corresponding to 90% capacity retention. In contrast, the bare NCM85 cell exhibited virtually linear capacity decay with cycling, with a specific capacity of 57 mAh/g after 200 cycles, resulting in only a 37% capacity retention. As for Coulombic efficiency (CE), DA-NCM85 showed a more rapid increase during the initial cycles and higher CE upon cycling than that of bare NCM85, indicating improved NCM85|LPSC interfacial stability. The long-term cycling at higher rates of 0.5C and 1C are shown in Figures S13 and S14, which also demonstrate improved long-term cycling stability after DA-coating. Their different electrochemical performance indicators are shown in the form of radar plots (Figure 3e). To investigate the effect of ethanol treatment on the cycling performance in material preparation, we also tested the cycling performance of ethanol-washed NCM85 (Figure S15). It also exhibits rapid capacity decay with a capacity retention of ∼55%. Even though the DA-NCM85 ASSBs performed well with a moderate cathode loading of 8−9 mg/cm^2, increasing the loading is necessary to match the area capacity of commercial LIBs (>3 mAh/cm^2). Thus, high-loading ASSBs (24.9 mg/cm^2 DA-NCM85) were constructed and tested in the voltage range of 2.0−4.2 V at 0.05C (∼0.25 mA/cm^2) using a prelithiated micron-sized Si anode $Li_{0.7}Si$ (Figure 3f and 3g). Micron-sized prelithiated Si ($Li_{0.7}Si$) can be employed as an alternative anode due to its high electrical conductivity, strong mechanical qualities, high specific capacity, and low potential.[43,44] Such a cell delivers an initial areal capacity of ∼4.4 mAh/cm^2 (specific capacity of ∼178 mAh/g) with an ICE of 86.3% and relatively stable capacity retention of 80% over 160 cycles.

To gain a deeper comprehension of the performance degradation caused by interfacial SE degradation, electrochemical impedance spectroscopy (EIS) was performed on various SSB cells after the 1st and 100th cycles. The results are shown in Figure 4a−d. The fitting results (the equivalent circuit model is shown in the inset of Figure 4a) show that both SSB cells have similar SE bulk resistance (R_{Bulk}) of about 45 Ω, referred to as an SE separator resistance.[45,46] The SE grain boundary resistance (R_{GB}) was estimated to be between 10 and 30 Ω. Note that this deviation results from local electrode inhomogeneities and some variation among the cell testing. The interfacial SE/CAM resistance ($R_{CAM/SE}$) was around 220 Ω after the first cycle for the bare NCM85 cell, compared to ∼105 Ω for the DA-NCM85 cell. The higher interfacial SE/CAM resistance for bare-NCM85 compared to DA-NCM85 after the initial cycle reveals much significant argyrodite decomposition. After 100 cycles, the $R_{CAM/SE}$ of the bare NCM85 cell grew more than 2-fold (448 Ω), whereas the $R_{CAM/SE}$ of DA-NCM85 cell only marginally increased to 115 Ω. These findings are consistent with the results observed in the electrochemical cycling and confirm the effectiveness of the nanometric coating layer in suppressing the argyrodite decomposition and thus buildup of high-resistance interphases.

The prevention of side reactions by this protective coating is further proven by *ex situ* XPS analysis of the chemical nature of the degradation products. Figure 4e−h shows the S 2*p* and P 2*p* XPS spectra of the bare NCM85 and DA-NCM85 cells after 200 cycles. The S $2p_{3/2}$ peak at 160.3 eV (green shading) present in the S 2*p* XPS spectra for both samples (Figure 4e,f) corresponds to the PS_4^{3-} moieties in the argyrodite. The other two major components (pink and red shading) in the S 2*p* XPS spectra of bare NCM85 (Figure 4f) correspond to P−S−P species at 161.7 eV ($P_2S_8^{4-}$, P_2S_x) and −S−S− species at 163.6 eV ("S^0" like long-chain polysulfides) due to oxidation of S^{2-}.[47] For DA-NCM85, there are virtually no peaks corresponding to oxidized sulfur species (Figure 4e). The P $2p_{3/2}$ peak at 132.4 eV (green shading, Figure 4g,h) in the P 2*p* spectrum of both samples is also characteristic of PS_4^{3-} units. In bare NCM85 (Figure 4h), another new feature at a higher binding energy (133.9 eV; characteristic of P_xO_y species in pink shading) is also apparent. These oxygenated phosphorus species can be associated with interfacial reactions between the CAM and SE.[48] The weak P 2*p* signal for DA-NCM85 (Figure 4g) could be attributable to the coating layer on the NCM being transferred to the next-neighbor argyrodite particles in the densified composite cathode due to the soft nature of waxy DA, thus obscuring the signal from the PS_4 groups in the argyrodite. The C 1*s* spectra (Figure S16a,b) show higher C−C/C−H intensity for the DA-coated NCM85 composite indicating the DA-coating is retained after 200 cycles, and thus it is stable at the upper voltage cutoff. Taken as a whole, the XPS spectra (especially S 2*p*) clearly demonstrate the occurrence of sulfide (argyrodite) oxidation in bare NCM85 cells is greatly suppressed by the DA coating. The stable interface between DA-NCM85/argyrodite clearly leads to the observed enhanced electrochemical performance described above.

In summary, we present an effective coating concept employing an organic fatty acid-derived "Li soap" on the cathode surface to stabilize against oxidative degradation of a sulfide solid electrolyte with high voltage cathodes in sulfide-electrolyte all-solid-state batteries. Utilizing a simple treatment of NCM85 with decanoic acid forms a nanometric coating layer via an acid−base reaction with the residual carbonate/hydroxide on the oxide surface. Notably, the entire treatment process is conducted under an ambient atmosphere and does not require high-temperature sintering. This makes mass production and commercialization viable while keeping the costs low. This coating acts as a conformal, nonrigid, and highly effective artificial cathode−electrolyte interphase that effectively stabilizes the argyrodite against oxidation. Accordingly, DA-NCM85 ASSB, utilizing a Li_6PS_5Cl electrolyte at typical cell loading level of ∼1.8 mAh/cm^2, exhibits a significantly improved capacity retention of 90% after 200 cycles at room temperature, which is more than 3-fold higher than that of a bare NCM85 ASSB. Furthermore, DA-coated NCM85 ASSB with a high loading of 24.9 mg/cm^2 exhibits a reversible capacity of ∼4.4 mAh/cm^2 and satisfactory cycling stability over 160 cycles. This work emphasizes the suitability and potential of this facile coating concept in suppressing interfacial degradation in sulfide-based composite cathodes.

https://doi.org/10.1021/acsenergylett.3c01717
ACS Energy Lett. 2023, 8, 4949−4956

■ ASSOCIATED CONTENT

Supporting Information

The Supporting Information is available free of charge at https://pubs.acs.org/doi/10.1021/acsenergylett.3c01717.

Experimental methods, Nyquist plots, electrochemical data, SEM, TEM (PDF)

■ AUTHOR INFORMATION

Corresponding Author

Linda F. Nazar − *Department of Chemistry and the Waterloo Institute for Nanotechnology, University of Waterloo, Waterloo, Ontario N2L 3G1, Canada; Joint Center for Energy Storage Research, Argonne National Laboratory, Argonne, Illinois 60439, United States;* orcid.org/0000-0002-3314-8197; Email: lfnazar@uwaterloo.ca

Authors

Yangyang Huang − *Department of Chemistry and the Waterloo Institute for Nanotechnology, University of Waterloo, Waterloo, Ontario N2L 3G1, Canada*

Laidong Zhou − *Department of Chemistry and the Waterloo Institute for Nanotechnology, University of Waterloo, Waterloo, Ontario N2L 3G1, Canada; Joint Center for Energy Storage Research, Argonne National Laboratory, Argonne, Illinois 60439, United States;* orcid.org/0000-0002-8556-3296

Chang Li − *Department of Chemistry and the Waterloo Institute for Nanotechnology, University of Waterloo, Waterloo, Ontario N2L 3G1, Canada; Joint Center for Energy Storage Research, Argonne National Laboratory, Argonne, Illinois 60439, United States;* orcid.org/0000-0001-5420-3856

Zhuo Yu − *Department of Chemistry and the Waterloo Institute for Nanotechnology, University of Waterloo, Waterloo, Ontario N2L 3G1, Canada*

Complete contact information is available at: https://pubs.acs.org/10.1021/acsenergylett.3c01717

Author Contributions

[§]Y.H. and L.Z. contributed equally to this work.

Notes

The authors declare no competing financial interest.

■ ACKNOWLEDGMENTS

LFN gratefully acknowledges NSERC via their Canada Research Chair and Discovery Grant programs and the Ontario Research Fund (ORF-RE) for financial support. Partial support (to L. Zhou and C. Li) was provided by the Joint Center for Energy Storage Research. We thank BASF-SE for supplying the polycrystalline NCM85 cathode material.

■ REFERENCES

(1) Trahey, L.; Brushett, F. R.; Balsara, N. P.; Ceder, G.; Cheng, L.; Chiang, Y. M.; Hahn, N. T.; Ingram, B. J.; Minteer, S. D.; Moore, J. S.; et al. Energy storage emerging: a perspective from the joint center for energy storage research. *Proc. Natl. Acad. Sci. U.S.A.* **2020**, *117* (23), 12550−12557.

(2) Bauer, C.; Burkhardt, S.; Dasgupta, N. P.; Ellingsen, L. A. W.; Gaines, L. L.; Hao, H.; Hischier, R.; Hu, L.; Huang, Y.; Janek, J.; et al. Charging sustainable batteries. *Nat. Sustain.* **2022**, *5*, 176−178.

(3) Randau, S.; Weber, D. A.; Kötz, O.; Koerver, R.; Btaun, P.; Weber, A.; Ivers-Tiffée, E.; Adermann, T.; Kulisch, J.; Zeier, W. G.; et al. Benchmarking the performance of all-solid-state lithium batteries. *Nat. Energy* **2020**, *5*, 259−270.

(4) Chen, R.; Li, Q.; Yu, X.; Chen, L.; Li, H. Approaching practically accessible solid-state batteries: stability issues related to solid electrolytes and interfaces. *Chem. Rev.* **2020**, *120* (14), 6820−6877.

(5) Zhang, Z.; Shao, Y.; Lotsch, B.; Hu, Y. S.; Li, H.; Janek, J.; Nazar, L. F.; Nan, C. W.; Maier, J.; Armand, M.; et al. New horizons for inorganic solid state ion conductors. *Energy Environ. Sci.* **2018**, *11*, 1945−1976.

(6) Bachman, J.; Muy, S.; Grimaud, A.; Chang, H. H.; Pour, N.; Lux, S. F.; Paschos, O.; Maglia, F.; Lupart, S.; Lamp, P.; et al. Inorganic solid state electrolytes for lithium batteries: mechanisms and properties governing ion conduction. *Chem. Rev.* **2016**, *116*, 140−162.

(7) Kwak, H.; Wang, S.; Park, J.; Liu, Y.; Kim, K. T.; Choi, Y.; Mo, Y.; Jung, Y. S. Emerging halide superionic conductors for all-solid-state batteries: design, synthesis, and practical applications. *ACS Energy Lett.* **2022**, *7* (5), 1776−1805.

(8) Kamaya, N.; Homma, K.; Yamakawa, Y.; Hirayama, M.; Kanno, R.; Yonemura, M.; Kamiyama, T.; Kato, Y.; Hama, S.; Kawamoto, K.; et al. A lithium superionic conductor. *Nat. Mater.* **2011**, *10* (9), 682−686.

(9) Kato, Y.; Hori, S.; Saito, T.; Suzuki, K.; Hirayama, M.; Mitsui, A.; Yonemura, M.; Iba, H.; Kanno, R. High-power all-solid-state batteries using sulfide superionic conductors. *Nat. Energy* **2016**, *1* (4), 16030.

(10) Zhou, L.; Assoud, A.; Zhang, Q.; Wu, X.; Nazar, L. F. New family of argyrodite thioantimonate lithium superionic conductors. *J. Am. Chem. Soc.* **2019**, *141* (48), 19002−19013.

(11) Li, Y.; Song, S.; Kim, H.; Nomoto, K.; Kim, H.; Sun, X.; Hori, S.; Suzuki, K.; Matsui, N.; Hirayama, M.; Mizoguchi, T.; Saito, T.; Kamiyama, T.; Kanno, R. A lithium superionic conductor for millimeter-thick battey electrode. *Science* **2023**, *381*, 50−53.

(12) Wenzel, S.; Sedlmaier, S. J.; Dietrich, C.; Zeier, W. G.; Janek, J. Interfacial reactivity and interphase growth of argyrodite solid electrolytes at lithium metal electrodes. *Solid State Ionics* **2018**, *318*, 102−112.

(13) Walther, F.; Koerver, R.; Fuchs, T.; Ohno, S.; Sann, J.; Rohnke, M.; Zeier, W. G.; Janek, J. Visualization of the interfacial decomposition of composite cathodes in argyrodite-based all-solid-state batteries using time-of-flight secondary-ion mass spectrometry. *Chem. Mater.* **2019**, *31* (10), 3745−3755.

(14) Ohno, S.; Rosenbach, C.; Dewald, G. F.; Janek, J.; Zeier, W. G. Linking solid electrolyte degradation to charge carrier transport in the thiophosphate-based composite cathode toward solid-state lithium-sulfur batteries. *Adv. Funct. Mater.* **2021**, *31* (18), 2010620.

(15) Kwok, C. Y.; Xu, S.; Kochetkov, I.; Zhou, L.; Nazar, L. F. High-performance all-solid-state Li_2S batteries using an interfacial redox mediator. *Energy Environ. Sci.* **2023**, *16*, 610−618.

(16) Culver, S. P.; Koerver, R.; Zeier, W. G.; Janek, J. On the Functionality of Coatings for Cathode Active Materials in Thiophosphate-Based All-Solid-State Batteries. *Adv. Energy Mater.* **2019**, *9*, 1900626.

(17) Tian, Y. S.; Shi, T.; Richards, W. D.; Li, J. C.; Kim, J. C.; Bo, S. H.; Ceder, G. Compatibility issues between electrodes and electrolytes in solid-state batteries. *Energy Environ. Sci.* **2017**, *10*, 1150−1166.

(18) Xiao, Y. H.; Miara, L.; Wang, Y.; Ceder, G. Computational Screening of Cathode Coatings for Solid-State Batteries. *Joule* **2019**, *3*, 1252−1275.

(19) Wang, C. H.; Liang, J. W.; Zhao, Y.; Zheng, M.; Li, X. N.; Sun, X. L. All-solid-state lithium batteries enabled by sulfide electrolytes: from fundamental research to practical engineering design. *Energy Environ. Sci.* **2021**, *14*, 2577−2619.

(20) Kim, A.-Y.; Strauss, F.; Bartsch, T.; Teo, J. H.; Hatsukade, T.; Mazilkin, A.; Janek, J.; Hartmann, P.; Brezesinski, T. Stabilizing Effect of a Hybrid Surface Coating on a Ni-Rich NCM Cathode Material in All-Solid-State Batteries. *Chem. Mater.* **2019**, *31* (23), 9664−9672.

(21) Takada, K.; Ohta, N.; Zhang, L. Q.; Fukuda, K.; Sakaguchi, I.; Ma, R. Z.; Osada, M.; Sasaki, T. Interfacial modification for high-power solid-state lithium batteries. *Solid State Ionics* **2008**, *179*, 1333−1337.

(22) Zhang, W.; Weber, D. A.; Weigand, H.; Arlt, T.; Manke, I.; Schroder, D.; Koerver, R.; Leichtweiss, T.; Hartmann, P.; Zeier, W. G.; Janek, J. *ACS Appl. Mater. Interfaces* **2017**, *9*, 17835−17845.
(23) Zhang, Y. Q.; Tian, Y. S.; Xiao, Y. H.; Miara, L.; Aihara, Y. C.; Tsujimura, T.; Shi, T.; Scott, M. C.; Ceder, G. Direct Visualization of the Interfacial Degradation of Cathode Coatings in Solid State Batteries: A Combined Experimental and Computational Study. *Adv. Energy Mater.* **2020**, *10*, 1903778.
(24) Sakuda, A.; Kitaura, H.; Hayashi, A.; Tadanaga, K.; Tatsumisago, M. J. All-solid-state lithium secondary batteries with oxide-coated $LiCoO_2$ electrode and $Li_2S-P_2S_5$ electrolyte. *J. Power Sources* **2009**, *189*, 527−530.
(25) Seino, Y.; Ota, T.; Takada, K. High rate capabilities of all-solid-state lithium secondary batteries using $Li_4Ti_5O_{12}$-coated $LiNi_{0.8}Co_{0.15}Al_{0.05}O_2$ and a sulfide-based solid electrolyte. *J. Power Sources* **2011**, *196* (15), 6488−6492.
(26) Han, F. D.; Yue, J.; Chen, C.; Zhao, N.; Fan, X. L.; Ma, Z. H.; Gao, T.; Wang, F.; Guo, X. X.; Wang, C. S. Interphase Engineering Enabled All-Ceramic Lithium Battery. *Joule* **2018**, *2*, 497−508.
(27) Jung, S. H.; Oh, K.; Nam, Y. J.; Oh, D. Y.; Bruner, P.; Kang, K.; Jung, Y. S. Li_3BO_3-Li_2CO_3: rotationally designed buffering phase for sulfide all-solid-state batteries. *Chem. Mater.* **2018**, *30*, 8190−8200.
(28) Payandeh, S.; Strauss, F.; Mazilkin, A.; Kondrakov, A.; Brezesinski, T. Tailoring the $LiNbO_3$ coating of Ni-rich cathode materials for stable and high-performance all-solid-state batteries. *Nano Res. Energy* **2022**, *1*, No. e9120016.
(29) Shi, B. X.; Yusim, Y.; Sen, S.; Demuth, T.; Ruess, R.; Volz, K.; Henss, A.; Richter, F. H. Mitigating Contact Loss in Li_6PS_5Cl-Based Solid-State Batteries Using a Thin Cationic Polymer Coating on NCM. *Adv. Energy Mater.* **2023**, *13*, 2300310.
(30) Hu, G. R.; Fan, J.; Lu, Y.; Zhang, Y. J.; Du, K.; Peng, Z. D.; Li, L. Y.; Zhang, B. C.; Cao, Y. B. Surface Architecture Design of $LiNi_{0.8}Co_{0.15}Al_{0.05}O_2$ Cathode with Synergistic Organics Encapsulation to Enhance Electrochemical Stability. *ChemSusChem* **2020**, *13*, 5699−5710.
(31) Gao, M. Y.; Wang, Y. Y.; Cui, S. L.; Liu, S.; Gao, X. P.; Li, G. R. Organo-Soluble Decanoic Acid-Modified Ni-Rich Cathode Material $LiNi_{0.90}Co_{0.07}Mn_{0.03}O_2$ for Lithium-Ion Batteries. *ACS Appl. Mater. Interfaces* **2022**, *14*, 16348−16356.
(32) Noh, H. J.; Youn, S.; Yoon, C. S.; Sun, Y. K. Comparison of the structural and electrochemical properties of layered $Li[Ni_xCo_yMn_z]O_2$ (X = 1/3, 0.5, 0.6, 0.7, 0.8 and 0.85) cathode material for lithium-ion batteries. *J. Power Source* **2013**, *233*, 121−130.
(33) Pritzl, D.; Teufl, T.; Freiberg, A. T. S.; Strehle, B.; Sicklinger, J.; Sommer, H.; Hartmann, P.; Gasteiger, H. A. Washing of Nikle-rich cathode materials for lithium-ion batteries: towards a mechanistic understanding. *J. Electrochem. Soc.* **2019**, *166*, A4056−A4066.
(34) Li, Y.; Tan, C.; Qi, G.; Guo, J.; Wang, X.; Zhang, S. Decanoate conversion layer with improved corrosion protection for magnesium alloy. *Corros. Sci.* **2013**, *70*, 229−234.
(35) Wang, S. H.; Yue, J.; Dong, W.; Zuo, T. T.; Li, J. Y.; Liu, X.; Zhang, X. D.; Liu, L.; Shi, J. L.; Yim, Y. X.; Guo, Y. G. Tuning wettability of molten lithium via a chemical strategy for lithium metal anodes. *Nat. Commun.* **2019**, *10*, 4930.
(36) Lu, W.; Xie, K.; Chen, Z.; Xiong, S.; Pan, Y.; Zheng, C. A new co-solvent for wide temperature lithium ion battery electrolytes: 2,2,2-Trifluoroethyl n-caproate. *J. Power Sources* **2015**, *274*, 676−684.
(37) Wood, K. N.; Teeter, G. XPS on Li-battery-related compounds: analysis of inorganic SEI phases and a methodology for charge correction. *ACS Appl. Energy Mater.* **2018**, *1*, 4493−4504.
(38) Hekmatfar, M.; Kazzazi, A.; Eshetu, G. G.; Hasa, I.; Passerini, S. Understanding the electrode/electrolyte interface layer on the Li-rich nickel manganese cobalt layered oxide cathode by XPS. *ACS Appl. Mater. Interfaces* **2019**, *11*, 43166−43179.
(39) Aas, N.; Bowker, M. Adsorption and autocatalytic decomposition of acetic acid on Pd(110). *J. Chem. Soc., Farady Trans.* **1993**, *89*, 1249−1255.
(40) Koerver, R.; Ayhun, I.; Leuchtweiß, T.; Dietrich, C.; Zhang, W. B.; Binder, J. O.; Hartmann, P.; Zeier, W. G.; Janek, J. Capacity Fade in Solid-State Batteries: Interphase Formation and Chemomechanical Processes in Nickel-Rich Layered Oxide Cathodes and Lithium Thiophosphate Solid Electrolytes. *Chem. Mater.* **2017**, *29*, 5574−5582.
(41) Quemin, E.; Dugas, R.; Koc, T.; Hennequart, B.; Chometon, R.; Tarascon, J. M. Decoupling parasitic reactions at the positive electrode interfaces in argyrodite-based systems. *ACS Appl. Mater. Interfaces* **2022**, *14*, 49284−499294.
(42) Kim, U. H.; Ryu, H. H.; Kim, J. H.; Mucke, R.; Kaghazchi, P.; Yoon, C. S.; Sun, Y. K. Microstructure-Controlled Ni-Rich Cathode Material by Microscale Compositional Partition for Next-Generation Electric Vehicles. *Adv. Energy Mater.* **2019**, *9*, 1803902.
(43) Zhou, L. D.; Zuo, T. T.; Kwok, C. Y.; Kim, S. Y.; Assoud, A.; Zhang, Q.; Janek, J.; Nazar, L. F. High areal capacity, long cycle life 4 V ceramic all-solid-state Li-ion batteries enabled by chloride solid electrolytes. *Nat. Energy* **2022**, *7*, 83−93.
(44) Zhou, L.; Zuo, T. T.; Li, C.; Zhang, Q.; Janek, J.; Nazar, L. F. $Li_{3-x}Zr_x(Ho/Lu)_{1-x}Cl_6$ solid electrolytes enable ultrahigh-loading solid-state batteries with a prelithiated Si anode. *ACS Energy Lett.* **2023**, *8*, 3102−3111.
(45) Zuo, T. T.; Walther, F.; Ahmed, S.; Rueß, R.; Hertle, J.; Mogwitz, B.; Volz, K.; Janek, J. Formation of an Artificial Cathode−Electrolyte Interphase to Suppress Interfacial Degradation of Ni-Rich Cathode Active Material with Sulfide Electrolytes for Solid-State Batteries. *ACS Energy Lett.* **2023**, *8*, 1322−1329.
(46) Ohta, N.; Takada, K.; Zhang, L. Q.; Ma, R. Z.; Osada, M.; Sasaki, T. Enhancement of the High-Rate Capability of Solid-State Lithium Batteries by Nanoscale Interfacial Modification. *Adv. Mater.* **2006**, *18*, 2226−2229.
(47) Auvergniot, J.; Cassel, A.; Foix, D.; Viallet, V.; Seznec, V.; Dedryvère, R. Redox activity of argyrodite Li_6PS_5Cl electrolyte in all-solid-state Li-ion battery: An XPS study. *Solid State Ionics* **2017**, *300*, 78−85.
(48) Walther, F.; Strauss, F.; Wu, X. H.; Mogwitz, B.; Hertle, J.; Sann, J.; Rohnke, M.; Brezesinski, T.; Janek, J. The Working Principle of a $Li_2CO_3/LiNbO_3$ Coating on NCM for Thiophosphate-Based All-Solid-State Batteries. *Chem. Mater.* **2021**, *33*, 2110−2125.

https://doi.org/10.1021/acsenergylett.3c01717
ACS Energy Lett. 2023, 8, 4949−4956